IPEM
Institute of Physics and
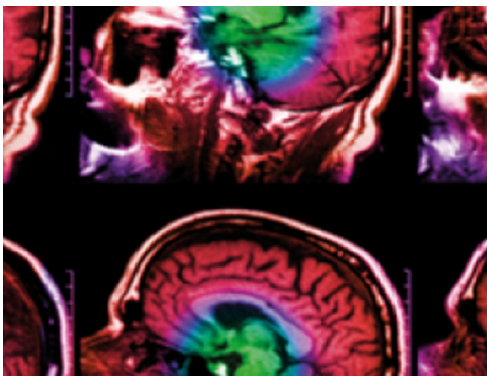Engineering in Medicine

PAPER • OPEN ACCESS

Dosimetric evaluation of off-axis fields and angular transmission for the 1.5 T MR-linac

To cite this article: M van den Dobbelsteen *et al* 2022 *Phys. Med. Biol.* **67** 205009

View the article online for updates and enhancements.

IPEM | IOP

Series in Physics and Engineering in Medicine and Biology

Your publishing choice in medical physics, biomedical engineering and related subjects.

Start exploring the collection–download the first chapter of every title for free.

Physics in Medicine & Biology

IPEM
Institute of Physics and
Engineering in Medicine

CrossMark

PAPER

Dosimetric evaluation of off-axis fields and angular transmission for the 1.5 T MR-linac

M van den Dobbelsteen [ID] , S L Hackett, J H W de Vries, B van Asselen, S Oolbekkink [ID] , S J Woodings and B W Raaymakers

Department of Radiotherapy, UMC Utrecht, Heidelberglaan 100, 3584 CX Utrecht, The Netherlands

E-mail: m.vandendobbelsteen-3@umcutrecht.nl

Abstract

Objective. GPU-oriented Monte Carlo dose (GPUMCD) is a fast dose calculation algorithm used for treatment planning on the Unity MR-linac. Treatments for the MR-linac must be calculated quickly and accurately, and must account for two important MR-linac aspects: off-axis positions and angular transmission through the cryostat, couch and MR-coils. Therefore, the aim of this research is to quantify the system-related errors for GPUMCD calculations over the range of clinically-relevant field configurations and gantry angles. *Approach.* Dose profiles (crossline, inline and PDD) were measured and calculated for varying field sizes, off-axis positions and depths. Eleven different (off-axis) positions were included. The angular transmission was investigated by measuring and calculating the transmission for multiple angles, taking the cryostat, couch and coils into account. *Main results.* Differences between absolute point doses were found to be within 1.7% for field sizes 2×2 cm^2 and larger. The relative dose profiles in the crossline, inline and PDD direction illustrated maximum mean dose differences of 0.9pp, 0.8pp and 0.7pp of D_{max} in the central region for field sizes 2×2 cm^2 and larger. The 1×1 cm^2 field size showed larger dosimetric errors for absolute point doses and relative dose profiles. The maximum mean DTA in the penumbra was 0.7 mm. The mean difference in angular transmission ranged from $-0.33\% \pm 0.60\%$ to $0.27\% \pm 0.91\%$ using three treatment machines. Additionally, 77.1%–93.7% of the datapoints remained within 1% transmission difference. The largest transmission differences were present at the edges of the table. *Significance.* This research showed that the GPUMCD algorithm provides reliable dose calculations with a low uncertainty for field sizes 2×2 cm^2 and larger, focusing on off-axis fields and angular transmission.
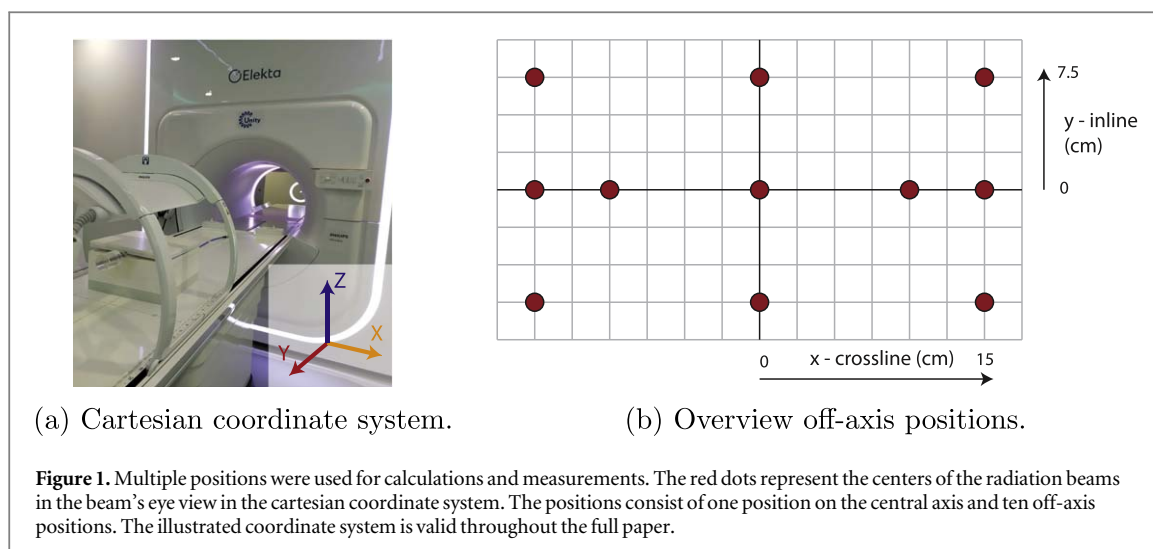
1. Introduction

Using MRI rather than cone-beam CT as an imaging modality during radiotherapy can result in images with better quality and soft tissue contrast (Chandarana *et al* 2018). This can improve the accuracy with which tumors can be targeted and therefore lead to a more accurate treatment, with beneficial outcomes for the patient. Therefore, the 1.5 T MR-linac has been developed, built and clinically introduced at UMC Utrecht (Raaymakers *et al* 2017). Two MR-linac systems are now commercially available: Unity (Elekta A.B., Stockholm, Sweden) (Raaymakers *et al* 2017) and MRIdian (Viewray, Cleveland, United States) (Acharya *et al* 2016). Alongside better imaging quality, this modern radiotherapy captures more frequently images of patients during treatment delivery to track anatomical changes (Winkel *et al* 2019). Currently, the MR-linac treatment plans are adapted at the start of each treatment while the patient is lying on the table. However, no quality assurance (QA) measurements are possible once the treatment workflow has started. Possibly, electronic portal imaging device (EPID) dosimetric verification could be used for daily QA (Bailey *et al* 2012, Zwan *et al* 2017, Torres-Xirau *et al* 2019). Additionally, logfiles could be used for daily patient QA, whereby it is important to prove that the dose calculations can be calculated accurately and that we can fully trust these outcomes as a base for the QA

procedure (Kontaxis *et al* 2020). An important feature of the MR-linac is that the system provides real-time anatomical feedback and this might offer the possibility for intra-fraction plan adaptations and real-time adaptive radiotherapy during the treatment in the future (Kontaxis *et al* 2017a, 2017b).

It must be ensured that the treatments for the MR-linac can be calculated and delivered quickly and accurately. Therefore Elekta developed a fast dose calculation algorithm, GPU-oriented Monte Carlo dose calculation platform (GPUMCD), to simulate the effects of the 1.5 T magnetic field for the Unity machine (Hissoiny *et al* 2011a, 2011b). The speed and accuracy with which plans can be calculated with the GPUMCD algorithm is critical to the safe delivery of adaptive radiotherapy. The impact of the magnetic field on the plan quality and dose distributions was already investigated earlier; including for example the effect of the magnetic field on the air gaps, the electron return effect, the electron streaming effect and effects on ionization chamber readings (Raaijmakers *et al* 2005, 2008, Hackett *et al* 2016, Agnew *et al* 2017, O'Brien and Sawakuchi 2017, Spindeldreier *et al* 2017, O'Brien *et al* 2018). Additionally, two important aspects of the MR-linac system must be considered when investigating the accuracy of the GPUMCD algorithm, as these settings are often used for MR-linac treatments and they differ substantially from the conventional linac systems. Firstly, there is a fixed isocenter which is often not in the center of the GTV, therefore fields are often delivered off-axis. It should be noted that this occurs in the *x*–*z* plane of the linac, while in the *y*-direction the target volumes are typically centered. However, on many sites multiple targets are irradiated, in which case at least one of the targets could be displaced along the *y*-axis. In this research, multiple (small) off-axis fields were measured and calculated. An investigation of the dosimetric and geometric accuracy of a single large field would not be indicative of the accuracy of small, off-axis fields, due to the change in the penumbra with off-axis position and field size. The penumbra/central region ratio is higher for smaller than larger fields. Secondly, the penumbra width is affected by the field size and the position, fields further off-axis have larger penumbras due to a larger scattering component (Mahmoudi *et al* 2019, Jelen *et al* 2020, Zhang *et al* 2021). Therefore, this research focuses both on the relative dose difference in the central region and on the distance to agreement (DTA) in the penumbra. The fields are not only defined by the off-axis output factors, which could be influenced by many factors, but also the off-axis fields are modeled differently (Sheikh-Bagheri and Rogers 2002, Chetty *et al* 2007) and should therefore also be verified during commissioning of the planning system and beam model (Ezzell *et al* 2003, Smilowitz *et al* 2015, Khan *et al* 2021). When focusing on off-axis positions, the scattering and transmission through the high-density beam delimiters (i.e. the MLCs and jaws) will be different for smaller fields compared to one larger field, and measuring smaller fields is more difficult, thereby potentially increasing the differences between measured and calculated doses (O'Brien *et al* 2018, Chen *et al* 2019). Secondly, the angular transmission is not uniform due to the cryostat, couch and coils. The MR-linac consists of the integrated MR base surrounded by the beam generating linac components. To minimize radiofrequency interference between the linac and the MRI scanner, the cryostat has been integrated into the Faraday cage (Tijssen *et al* 2019). The transmission through the cryostat, couch and MR-coils could influence the accuracy of the dose distribution, particularly as the Unity couch contains higher density components compared to a typical conventional linac couch (Woodings *et al* 2018b, Iakovenko *et al* 2020).

Recent studies already provided a comparison between GPUMCD against other algorithms and measurements (Ahmad *et al* 2016, Paudel *et al* 2016). These studies focused on fields on the central axis, whereas this study comprises a set of off-axis fields. Paudel *et al* and Ahmad *et al* both investigated the GPUMCD algorithm at different tissue interfaces; e.g. tumor/lung, tissue/lung, tissue/bone, and bone/titanium (Ahmad *et al* 2016, Paudel *et al* 2016). Both studies showed a good agreement of the GPUMCD algorithm against other measurements and algorithms at different tissue interfaces. Therefore, this study only focused on dose profiles in a water phantom without any tissue interfaces. This research will give an overview of the sources of uncertainty related to the treatment unit specifically important for the MR-linac treatments, which differ from the conventional linac systems. These specific aspects, comprising dose profiles with different field-sizes, different off-axis positions and different depths, as well as the angular transmission, influenced by the cryostat, couch and coils, have not been investigated before. The previous studies do not reflect the typical field sizes and positions that will be used for clinical treatment and the accuracy of calculations as a function of gantry angle has been previously investigated in the context of the commissioning of a Unity system (Snyder *et al* 2020). However, this study will distinguish between the contributions of each high-density component to the beam attenuations. Additionally, this study will give an overview of the variation of different transmission datasets, which has not been illustrated before. The aim of this research is to determine the system-related uncertainty for GPUMCD calculations using clinically-relevant field configurations and gantry angles for the MR-linac.

(a) Cartesian coordinate system.   (b) Overview off-axis positions.

Figure 1. Multiple positions were used for calculations and measurements. The red dots represent the centers of the radiation beams in the beam's eye view in the cartesian coordinate system. The positions consist of one position on the central axis and ten off-axis positions. The illustrated coordinate system is valid throughout the full paper.

2. Material and methods

2.1. Off-axis dose distributions

The dosimetric uncertainties arising from the GPUMCD algorithm were investigated using the Monaco treatment planning system (TPS) (Elekta A.B., Stockholm, Sweden). The dosimetric differences between measurements and GPUMCD calculations were examined, focusing on both the absolute and relative dose differences. Varying the field size, off-axis positions and depths for measurements and calculations lead to the dosimetric uncertainty from the calculation at each point in the calculated dose grid. The dosimetric uncertainties were determined for field sizes varying from 1×1 cm^2 to 22×40 cm^2. Field sizes 1×1 cm^2, 2×2 cm^2, 3×3 cm^2, 4×4 cm^2, 5×5 cm^2 and 10×10 cm^2 were measured on the central axis as well as at multiple off-axis positions. The 5×5 cm^2 field was measured on the central axis and ten positions away from the central axis, illustrated in figure 1. The Beamscan MR Watertank (PTW, Freiburg, Germany) was used for these calculations and measurements with a gantry angle of 0°and an SSD of 133.5 cm. Lastly, measurements were performed at a depth of 13 mm, 50 mm and 100 mm. The origin was positioned at the central axis on the water surface. Two MR-linac Unity systems with their specific beam models were used for the measurements.

2.1.1. Calculations of off-axis dose distributions

The Monaco TPS (v5.40.01 and v5.51.10) was used to calculate the 3D dose grid for multiple field sizes, off-axis positions and depths. It should be noted that there was no modification to the GPUMCD algorithm between these two versions. The smallest field size used to commission the Monaco beam model is 1×1 cm^2. For field sizes equal to or smaller than 3×3 cm^2 the plans were calculated with a grid size of 0.1 cm with 0.2% statistical uncertainty per field with 1 SD in the high dose area. For larger field sizes a grid size of 0.1 cm with 0.5% statistical uncertainty per field was used. The relative dose profiles were normalized using the median dose out of five data points in the center of the beam.

2.1.2. Measurements of off-axis dose distributions

The Beamscan MR Watertank (PTW T93001 SN 181 189 and PTW T41053 SN 171 869) was used to measure the dosimetric outcome over the range of field sizes, off-axis positions and depths. The watertank is MR compatible and the machine can be operated from outside the machine room. The watertank is commercially available and is used for commissioning and QA of the MR-linac, with a scanning range of 568 mm $\times$ 355 mm $\times$ 145 mm.

The setup and alignment of the watertank was the essential first step, where plastic holders were used for the positioning of the watertank in the center of the table. A plate with ball bearings was positioned at the base of the watertank and an EPID was used to image this plate using Elekta's MVIC software. The QA alignment software from Elekta was used to find the displacement in the x-direction and the rotation about the z-axis for the tank itself. Levelling took place whereby the water sensor measured four different locations to compensate for the rotation around the x-axis and the y-axis. The watertank scanning mechanism is oriented parallel to the water surface and has two identical holders for the detectors. For fields far off-center in the negative x-direction, the first detector position was used and for fields far off-center in the positive x-direction, the second detector position was used. For larger fields, both detector positions were used in the crossline direction and the active

detector which is used to measure the dose switches at $x = 1$ mm. Consequently, these larger dose profiles consist of two combined measurements measured with two detectors.

For relative dosimetry Microdiamond detectors (PTW TW60019 SN 123 758-123759) were used in the two holder positions. For fields larger than 3×3 cm^2 a Semiflex 3D reference chamber was used to correct for variabilities in the dose rate (PTW TW31021 SN 142 584). For correct positioning of the detectors, holders with ball bearings were positioned in the watertank and an EPID was used to image these holders with ball bearings. The QA alignment software from Elekta was used to find the offset in the x, y and z-direction from the ball bearings to the watertank isocenter. The Beamscan software from PTW (WaterTankScans Version 4.5) produced profiles in parallel directions to find the final rotation of the radiation field with respect to the watertank and compensates for this difference. The relative dose profiles were acquired with different step sizes for the crossline and inline dose profiles. For the outer region, penumbra and central regions of the field, step sizes of 3 mm, 0.5 mm and 0.5 mm (1×1 cm^2, 2×2 cm^2, 3×3 cm^2), 3 mm, 1 mm and 1 mm (4×4 cm^2, 5×5 cm^2), 2 mm, 2 mm and 2 mm (10×10 cm^2) and 4 mm, 2 mm and 4 mm ($>10 \times 10$ cm^2) were used, respectively. The relative dose profiles were again normalized using the median dose out of five data points in the center of the beam. For PDD profiles the step size was 1 mm for the depths from -10 to 25 mm from the origin and a step size of 2 mm for depths deeper than 25 mm. For the off-axis fields the PDD profiles were measured along the divergent path of the beam.
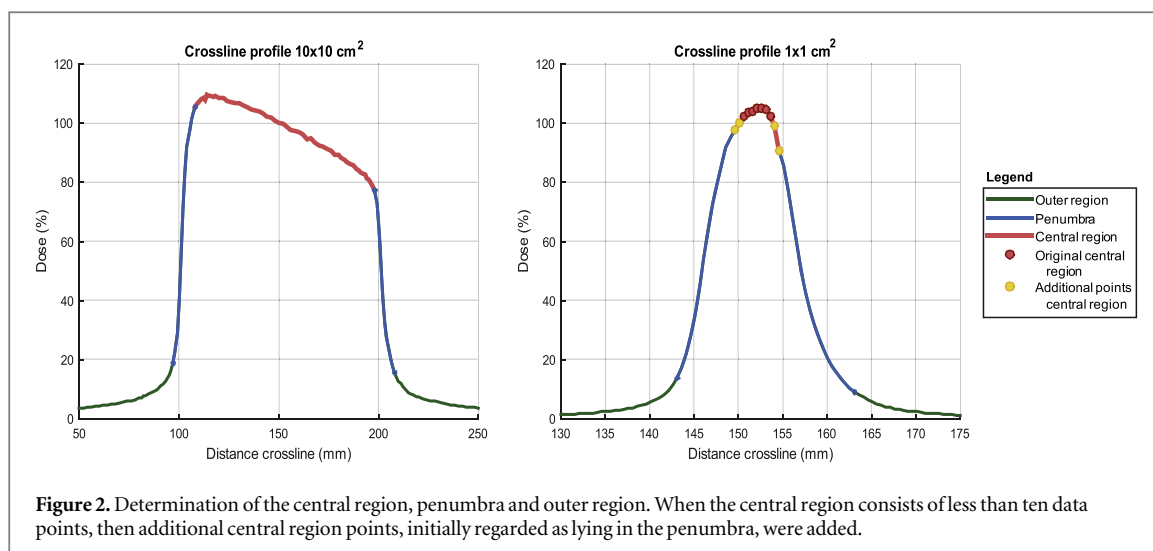
For absolute dosimetry the Microdiamond detector (PTW TW60019 SN 123 758) was used with an angular dependency correction illustrated by Woodings *et al* (Woodings *et al* 2018a). For the smallest field sizes of 1×1 cm^2 and 2×2 cm^2, correction factors of 0.984 and 0.997 for the relative output factors of the Microdiamond were respectively applied (Palmans *et al* 2018). The reference conditions for absolute dosimetry were used where the dose was normalised to an expected dose in a 10×10 cm^2; for the specific MR-linac this was 69.8 cGy per 100 MU at a depth of 100 mm at the isocenter. 100 MU was irradiated for every radiation beam varying the field size, off-axis position and depth. Every measurement was performed twice and the final dose was averaged over these two measurements. Variation in the standard 10×10 cm^2 field due to environmental changes was used to correct the other readings. These standard fields were repeated after approximately ten readings.

The described positioning method for the watertank has an reproducibility of $\leqslant 0.1$ mm on one axis according to the vendor's specification. The MVIC is used to position the detectors and the uncertainty related to the MVIC is 0.2 mm/pixel. Additionally, the magnetic field affected the position of the effective point of measurement (EPOM) of the detectors (Woodings *et al* 2018a, O'Brien *et al* 2018). Consequently, the positioning error was determined and a shift was applied to the measured data to correct for the positioning error. The maximum shift for one of the measurement sessions was a crossline shift of 0.6 mm and an inline shift of 0.4 mm. A detailed explanation about the determination of the positioning error is described in the supplementary data.

2.1.3. Comparison calculation and measurement of off-axis dose distributions

The dosimetric outcome of calculations and measurements for the relative crossline, inline and PDD profiles were compared. To match the calculated data to the measured data, linear interpolation of the dose grid was applied in Matlab (Version 2019a, Natick, Massachusetts: The MathWorks Inc, USA). Every crossline and inline dose profile was divided in a central region, penumbra and outer region for further analysis. For all field sizes the second derivative was used to determine these three different regions as illustrated in figure 2. For the PDD profiles the central region consisted of all the points with a depth deeper than 13 mm, not taking the build-up region into account. For the fields with a field size of 1×1 cm^2, only a small central region could be determined using this method. In some cases the central region only consisted of two data points. In order to make a robust assessment of the accuracy of the calculations in this central region, the number of points in the central region was extended. A minimum of ten datapoints were selected by including points lateral to this central region, this is illustrated in figure 2. It should be noted that the extended central region consists partly of the penumbra, so including these high-dose gradient regions in the analysis can result in an over-estimation of the dose difference of the 'central' region for these fields. The mean relative dose differences in the central region were calculated for different field sizes and positions. In some cases, multiple measurements were available for the same field size and position, whereby the average dose difference was used. In the penumbra the relative dose differences appear to be larger compared to the central region, due to the steep dose gradient in the penumbra. Therefore, a DTA in the penumbra was determined between the dose profiles of the measurements and the calculations. To determine the DTA, the closest distance between each point in the dose profiles of measurements and calculations was found, whereby the relative dose difference was less than 0.1pp of $D_{\max}$. If it was not possible to find a point within this criterion, the dose difference criterion was relaxed to 0.25pp of $D_{\max}$. If no solution was found, the distance with the smallest dose difference was used. The absolute point dose differences were compared for measurements and calculations. The relative dose difference (in pp of $D_{\max}$) represents the

Figure 2. Determination of the central region, penumbra and outer region. When the central region consists of less than ten data points, then additional central region points, initially regarded as lying in the penumbra, were added.

calculated dose (in % of D_{max}) subtracted from the measured dose (in % of D_{max}). Finally, a global γ analysis was performed between measured and calculated relative dosimetric outcomes using a γ criterion of 2%/2 mm.
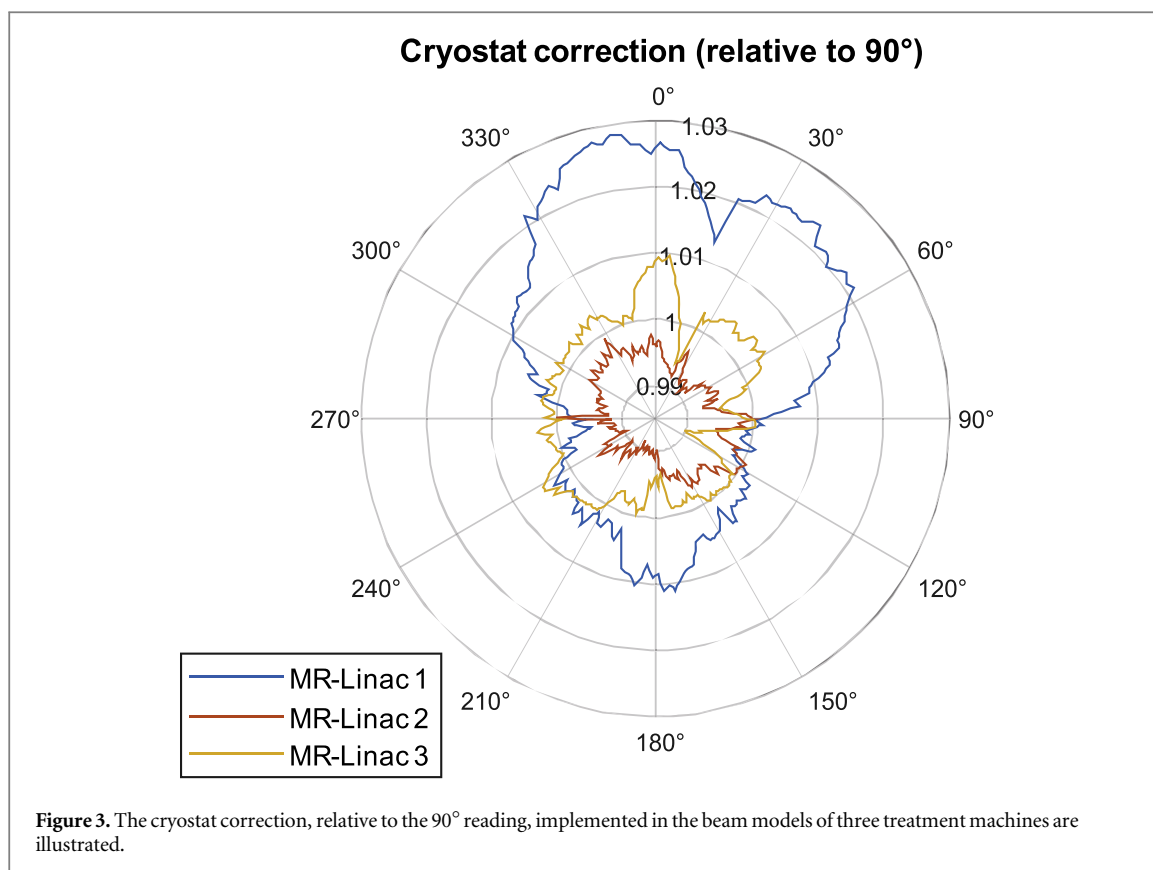
2.2. Angular transmission

The cryostat transmission is not uniform over the entire cryostat. To correct the output for this variation, the cryostat transmission as a function of the gantry angle is incorporated in the beam model. It should be noted that the cryostat transmission is always measured and commissioned around the axis of gantry rotation only and assumed to be isotropic in the *y*-direction. The transmission was measured and calculated, incorporating the effects of the anterior and posterior MR-coils, the Unity couch and the cryostat (van den Dobbelsteen *et al* 2022). The posterior coil is positioned directly below the table (Roberts *et al* 2021). The cryostat correction for three treatment machines is illustrated in figure 3. The first MR-linac was built earlier compared to the other treatment machines, showing higher cryostat corrections, as this machine was built using different welding and rolling techniques. The transmission was measured and calculated on a cylindrical phantom, with 100 MU per beam with a field size of 10×10 cm^2. The transmission was calculated and measured at intervals of 2°, 2.5°, 4° or 5°, depending on the dataset. The transmission of the cryostat, coils and couch model was normalized to the reading at gantry 90°, which is the gantry angle used for absolute dosimetry measurements.

2.2.1. Calculation of angular transmission

Calculations (0.2 cm grid size, uncertainty 0.5% per control point) in the Monaco TPS (v5.51.10) were performed with a cylindrical phantom (PMMA, RED 1.147, diameter 40 mm or 56 mm, according to the diameter of the build-up cap used for the measurement). The dose was determined as the mean dose in a sphere with a radius of 0.25 cm. The cryostat transmission, couch and coils were modeled and implemented standardly in Monaco. In some cases multiple calculations were available for the same angle and treatment machine, whereby the average value of these calculations was used. In general, the angles used for the measurements were also used for the calculations. Except when the measurements were performed every 2°, the calculations were carried out every 4°. Only, regions at the edge of the table, from 100° to 140° and from 220° to 260°, were calculated every 2°.

2.2.2. Measurement of angular transmission

The transmission was measured using a Farmer chamber (PTW TW30013 SN 008 377), whereby the detector was placed precisely in the middle of the bore using the cryostat characterization tool (CCT) from Elekta. The CCT consists of a holder to place the detector including a build-up cap and a mechanism to precisely displace the holder. Measurements were performed with water around the chamber to avoid any influence of small air volumes around the chamber on the chamber readings (Hackett *et al* 2016). The EPID was used to determine the detector position and the CCT gives the opportunity to precisely displace the detector position by manually turning screws, leading to the correct detector position. In total five different datasets were used on three different treatment machines. Two measurements both with and without anterior coil were used for MR-linac 1, two measurements with anterior coil were used for MR-linac 2 and one measurement with anterior coil was used for MR-linac 3. Secondly, the detector orientation differed per dataset. In some datasets the average reading of two orientations of the Farmer chamber was used. In the first orientation the longitudinal mark on the chamber

Figure 3. The cryostat correction, relative to the 90° reading, implemented in the beam models of three treatment machines are illustrated.

was orientated in the positive *z*-direction in the cartesian coordinate system. In the second orientation the chamber was rotated 180° on the *y*-axis. In other datasets, only the first orientation was used. Both one and two orientations were used for MR-linac 1 (two orientations for the first dataset), one orientation was used for two measurements for MR-linac 2 and one measurement with two orientations was used for MR-linac 3. The first dataset for the three machines was measured every 2°and the second dataset was measured every 5°or 2.5°(at parts of the table). The transmission of the cryostat, coils and couch model was normalized to the reading at gantry 90°. Readings at a gantry angle of 90°were used to account for variations of temperature, pressure and beam output. These standard fields were repeated after approximately ten readings.

2.2.3. Comparison calculation and measurement of angular transmission
The transmission of the cryostat, coils and couch model were verified, relative to the 90°reading, by comparing the calculations and measurements.

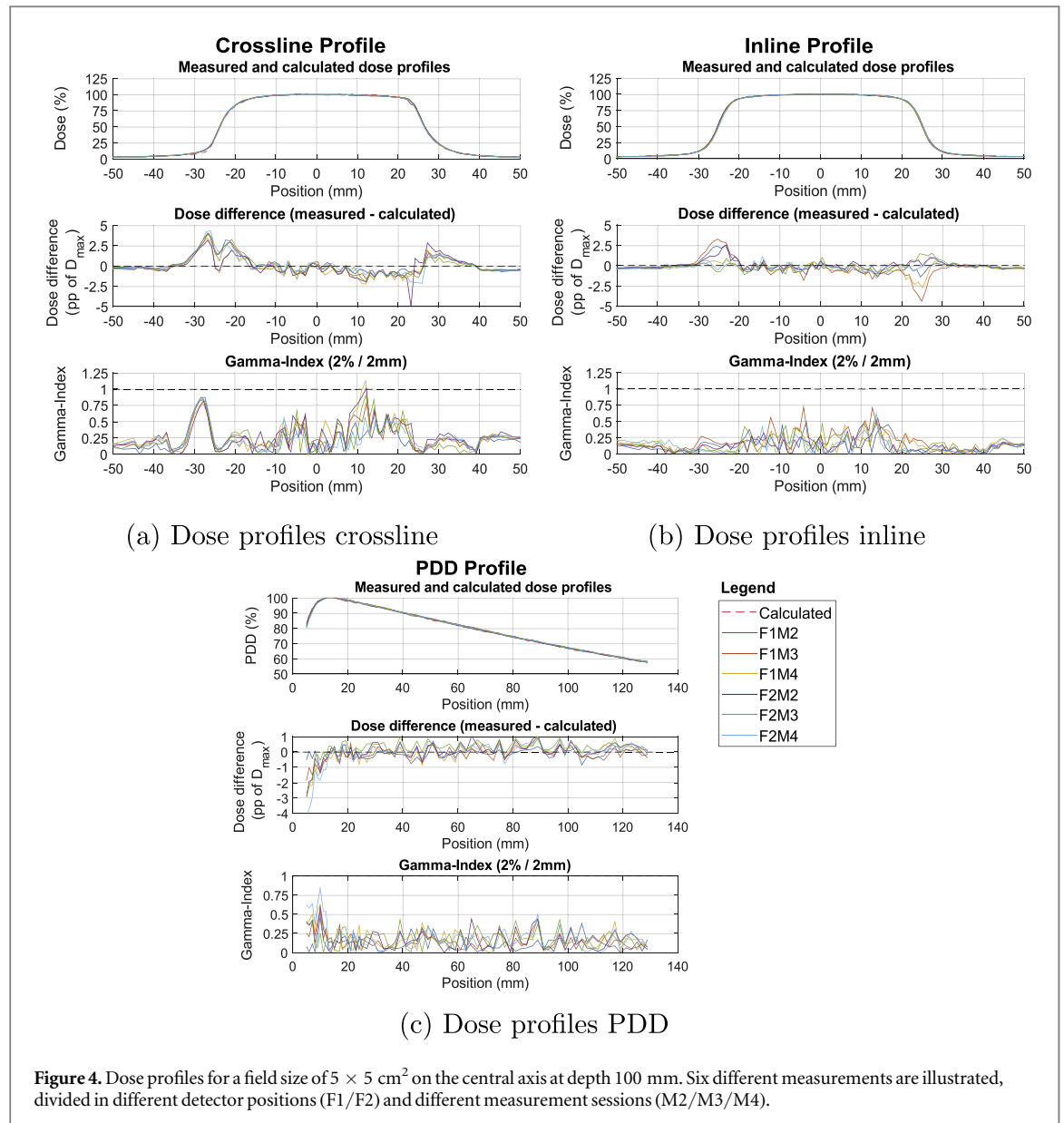## 3. Results

3.1. Off-axis dose distributions
Crossline, inline and PDD profiles from the measurements were compared to the 3D dose distributions from the TPS, varying the field size, position from the central axis and the depth.

3.1.1. Reproducibility
Figure 4 shows the relative dose profiles for a 5×5 cm^2 field on the central axis, at a depth of 100 mm. This figure illustrates a good agreement between measured and calculated profiles when looking at the dose difference and the γ index (2%/2 mm). The figure also shows good reproducibility of six different measurements, which were acquired in multiple sessions using the same measurement protocols and for the two different detector positions, F1 and F2. F1 and F2 represent the detector holder positions of the Beamscan MR Watertank that are needed to measure large fields in the crossline direction.

3.1.2. Depths
Relative dose profiles measured and calculated at depths of 13 mm, 50 mm and 100 mm were compared. Figure 5 illustrates that the dose differences in different depths show similar agreement between calculated and measured dose profiles. In the crossline direction, the dose differences in the central region are similar for

Figure 4. Dose profiles for a field size of 5×5 cm^2 on the central axis at depth 100 mm. Six different measurements are illustrated, divided in different detector positions (F1/F2) and different measurement sessions (M2/M3/M4).

different depths. There appears to be a trend of increasing maximum relative dose differences at shallower depths in the crossline direction around the shoulder of the profile, whereas no trend is evident in the inline profiles. The relative dose differences in inline direction are similar for the different depths, for both the central region as the penumbra. As there is no clear distinction between different depths, the remaining measurements and calculations were only investigated on the standard depth of 100 mm.
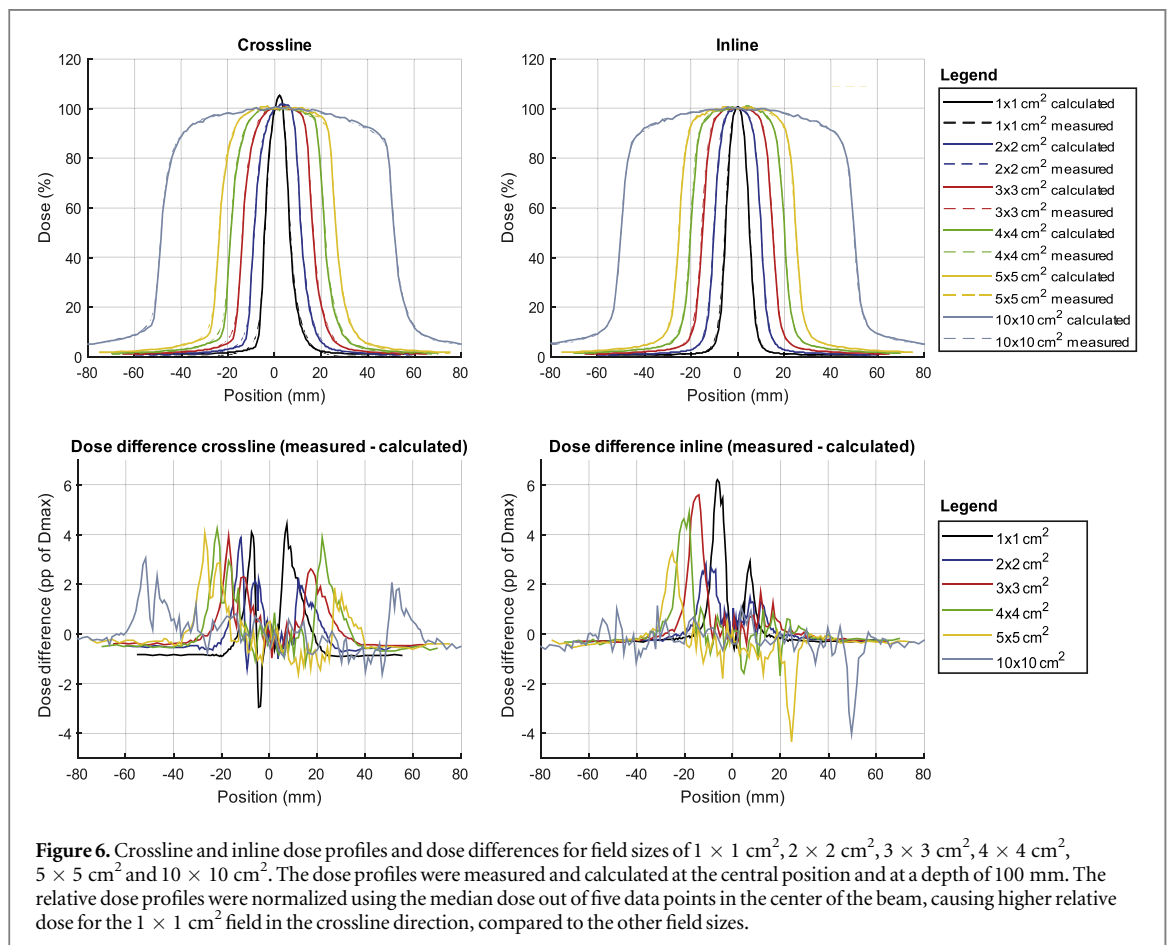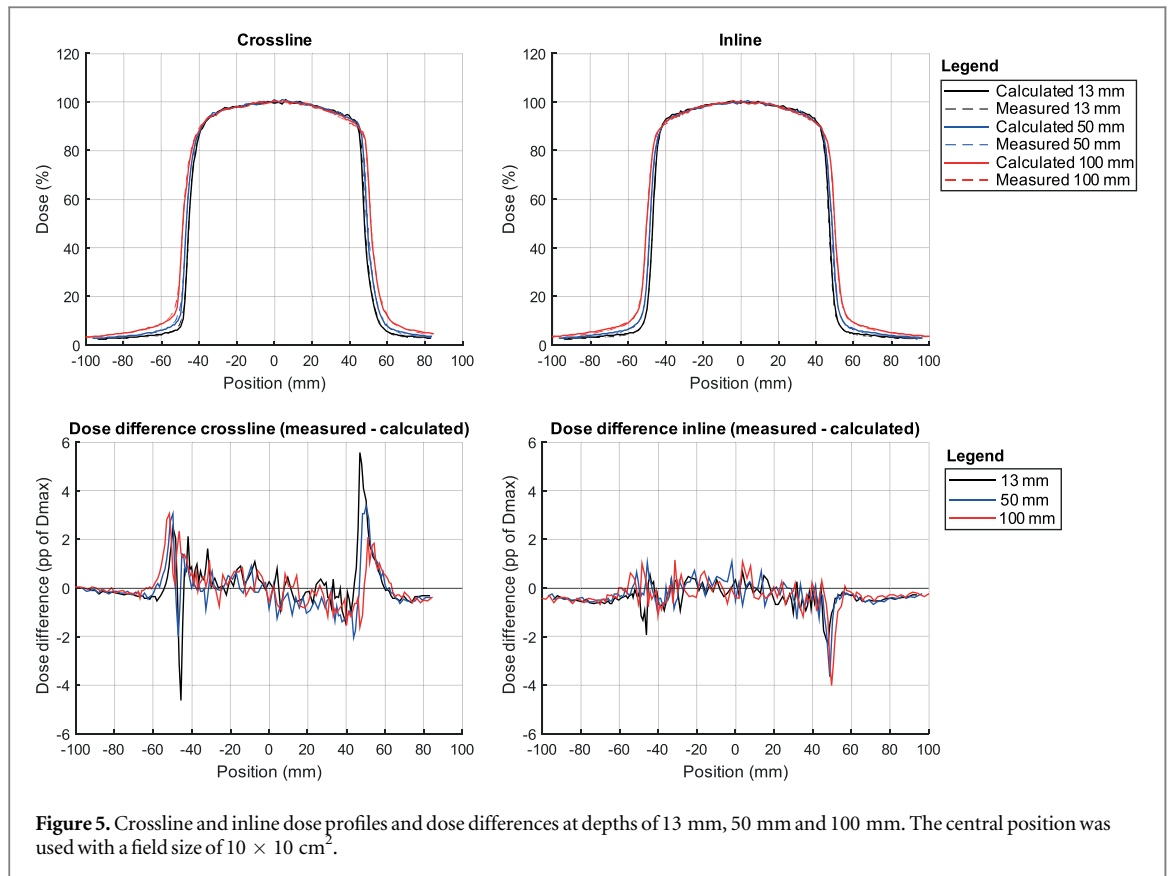
3.1.3. Field sizes

The crossline and inline dose profiles show good agreement between measured and calculated doses over the range of different field sizes, as illustrated in figure 6.

The relative dose differences in the crossline direction are similar for all field sizes. The highest dose differences are present in the penumbra with a similar range for the different field sizes. For the inline profiles the highest dose differences are again visible in the penumbra, with maximum relative dose differences of 6.2pp, 2.8pp, 5.6pp, 4.9pp, 4.4pp and 4.0pp of D_{max}, respectively for field sizes of 1×1 cm^2, 2×2 cm^2, 3×3 cm^2, 4×4 cm^2, 5×5 cm^2 and 10×10 cm^2. Fields with sizes larger than 10×10 cm^2 showed similar results.

3.1.4. Penumbra

Overall, the gamma criteria for a global 2%/2 mm were met for 57%–100% of the data points in the penumbra regions of the dose profiles, whereby 87% of the dose profiles had a gamma passing rate of 100%. In the right penumbra in the crossline and inline direction, all the points passed the gamma criteria. The relative dose differences showed larger values for the penumbra region compared to the central region. However, small shifts
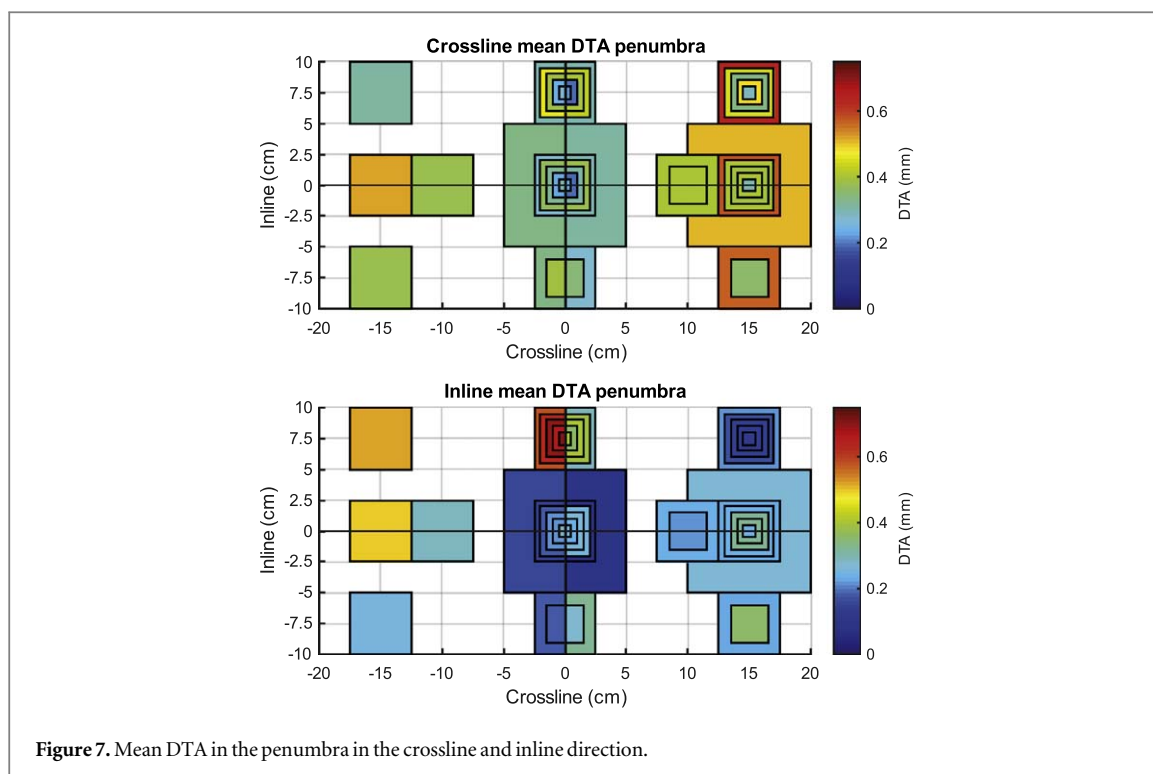
Figure 5. Crossline and inline dose profiles and dose differences at depths of 13 mm, 50 mm and 100 mm. The central position was used with a field size of 10×10 cm^2.

Figure 6. Crossline and inline dose profiles and dose differences for field sizes of 1×1 cm^2, 2×2 cm^2, 3×3 cm^2, 4×4 cm^2, 5×5 cm^2 and 10×10 cm^2. The dose profiles were measured and calculated at the central position and at a depth of 100 mm. The relative dose profiles were normalized using the median dose out of five data points in the center of the beam, causing higher relative dose for the 1×1 cm^2 field in the crossline direction, compared to the other field sizes.

Figure 7. Mean DTA in the penumbra in the crossline and inline direction.

in the profiles could already cause large dose differences due to a large dose gradient fall-off. The DTA is illustrated for the penumbra region in figure 7. The maximum mean DTA was 0.6 mm in the crossline direction and 0.7 mm in the inline direction. Positions further from the central axis or different field sizes did not show larger DTA values in the penumbra.

3.1.5. Off-axis positions

Positions further from the central axis or different field sizes do not show larger dosimetric errors for the relative dose profiles for field sizes 2×2 cm^2 and larger. In the following section the field sizes ranged from 2×2 cm^2 up to 10×10 cm^2. The 1×1 cm^2 fields showed considerably larger differences between calculated and measured doses and will be discussed separately. Figure 8 shows absolute point dose differences and relative dose differences (mean and standard deviation) in the central region for multiple field sizes and off-axis positions, all measured at a depth of 100 mm.
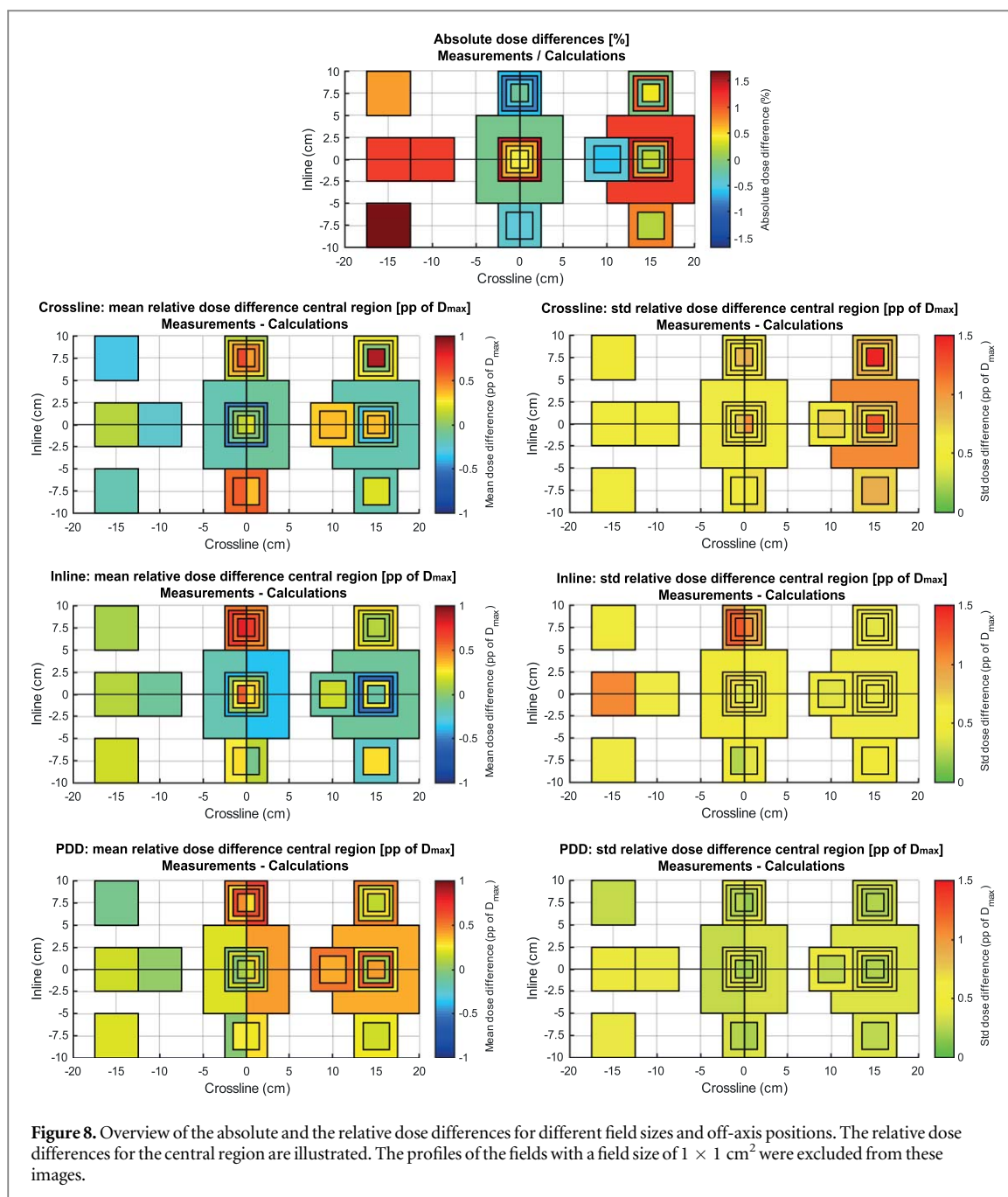
Absolute point doses. The absolute point dose differences between the measurements and the calculations ranged from -0.8% to 1.7%. The standard 10×10 cm^2 was used to normalise the readings, therefore the smaller field sizes in the central axis or fields further off-axis showed some larger deviations compared to the 10×10 cm^2 field.

Relative dose profiles. For the relative crossline dose profiles the mean dose difference in the central region ranged from -0.5pp ± 0.7pp (mean $\pm$ standard deviation) to 0.9pp ± 1.5pp of D_{max}. For the relative inline dose profiles the mean dose difference ranged from -0.5pp ± 0.6pp to 0.8pp ± 1.3pp of D_{max}. For the PDD profiles the mean dose difference ranged from -0.1pp ± 0.3pp to 0.7pp ± 0.4pp of D_{max}.

1×1 cm^2 field. The 1×1 cm^2 field sizes showed larger dose differences compared to the other field sizes. For the 1×1 cm^2 fields the absolute point dose differences between the measurements and the calculations ranged from 4.3% to 5.3%. For crossline, inline and PDD profiles the mean relative dose differences ranged from -0.2pp ± 0.6pp to 1.7pp ± 3.2pp, from -0.5pp ± 1.4pp to 1.7pp ± 2.1pp and from -0.3pp ± 0.4pp to 0.2pp ± 0.3pp of D_{max}, respectively.

3.2. Angular transmission

The measured transmission, calculated transmission and cryostat transmission for all three treatment machines are illustrated in figure 9. The figure shows a similar transmission as a function of gantry angle of the measurements and the calculations. The effect of the table is clearly visible from gantry angles of approximately $100°$ up to $260°$. From $0°$ to $50°$ and from $310°$ to $360°$ the anterior coil affects the transmission, introducing an attenuation of approximately 1%. This is clearly visible in figure 1(a) where the measurements were performed both with and without anterior coil. The cryostat transmission only takes the influence of the cryostat into account, there is no correction for the table and the coils.
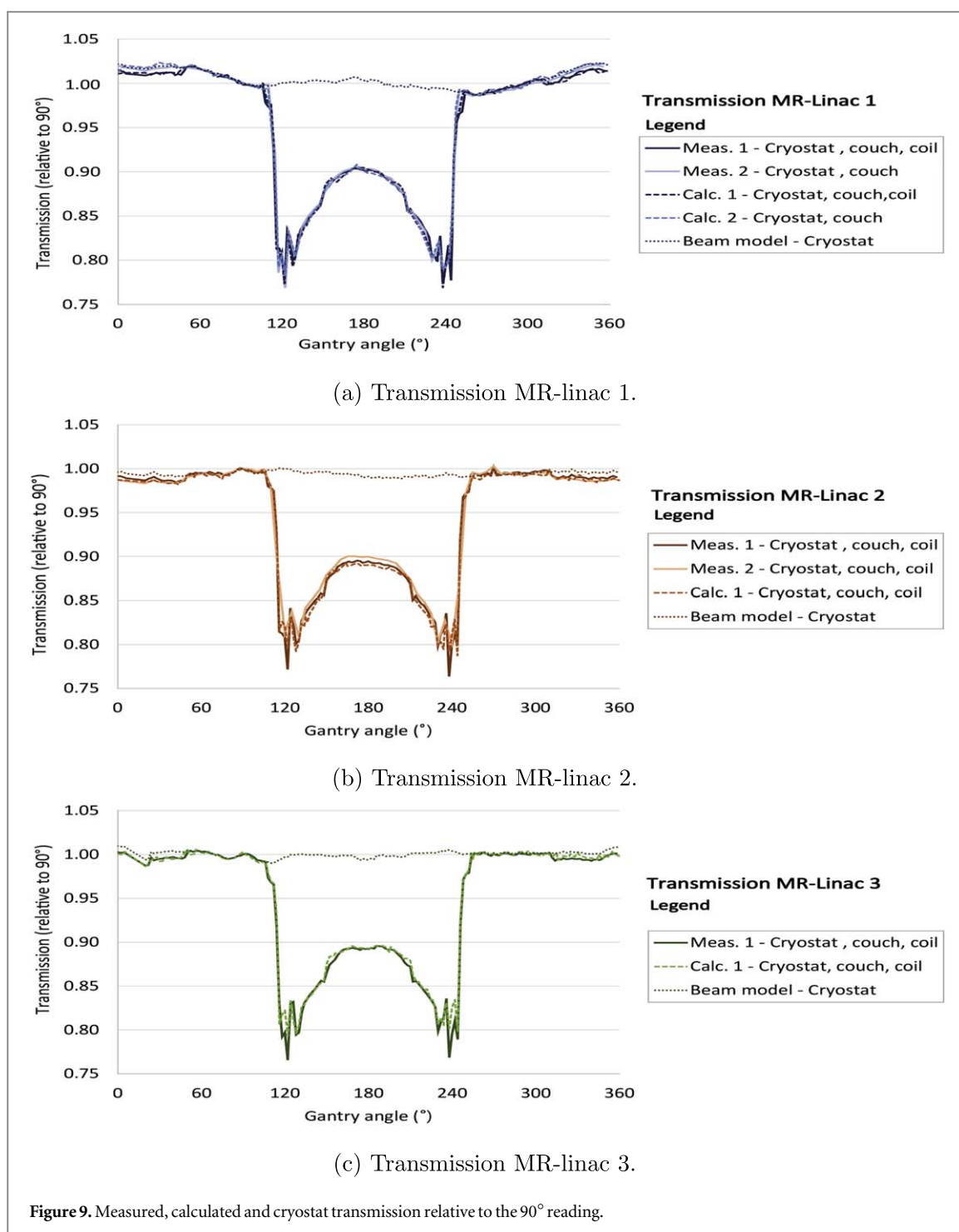
Figure 8. Overview of the absolute and the relative dose differences for different field sizes and off-axis positions. The relative dose differences for the central region are illustrated. The profiles of the fields with a field size of 1×1 cm^2 were excluded from these images.

3.2.1. Comparison calculations and measurements
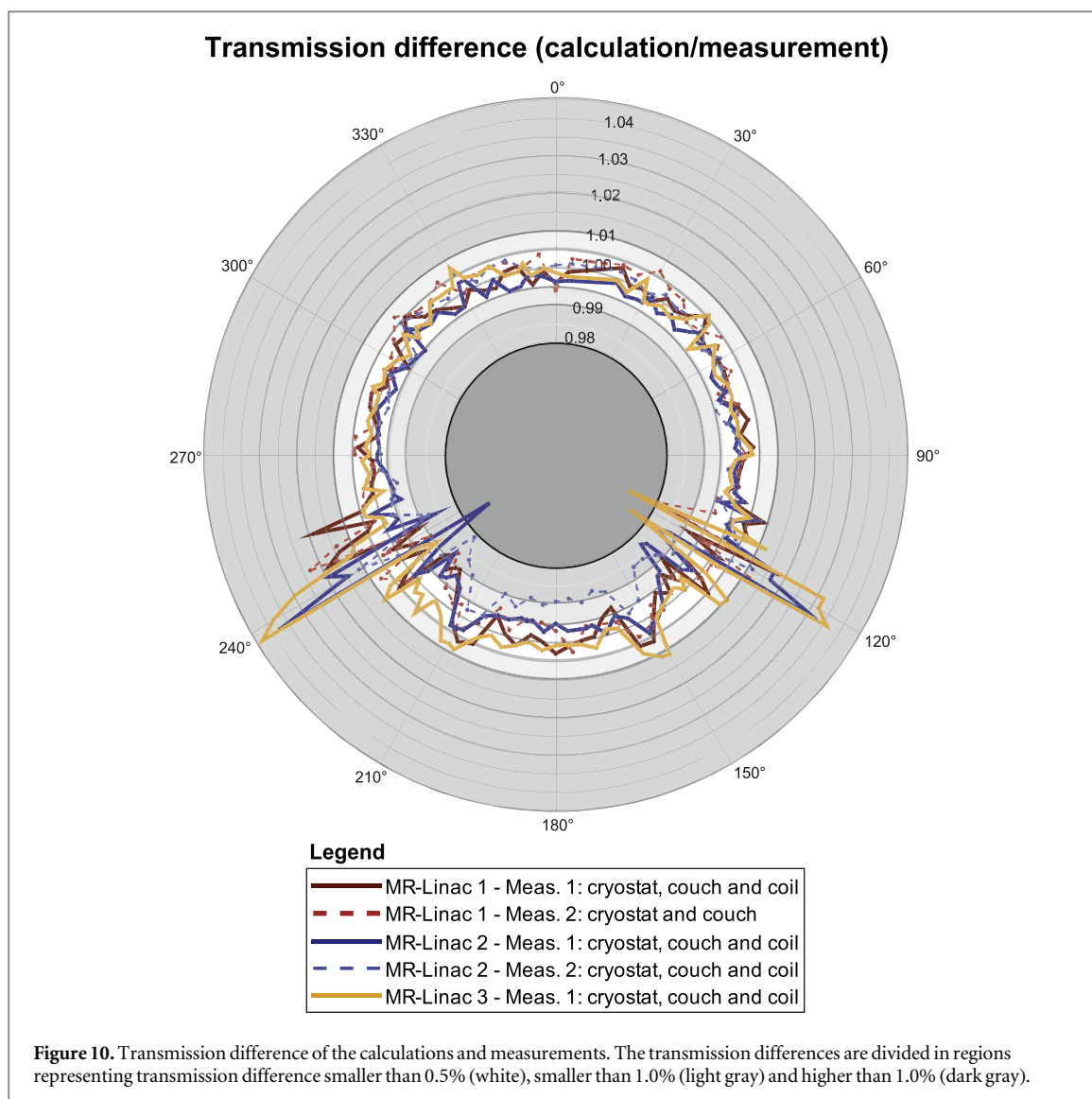
Figure 9 illustrates the agreement between the transmission (relative to 90°) of the calculations and measurements for different angles for three treatment machines. In total five different datasets were used: MR-linac 1 measurement 1, MR-linac 1 measurement 2 (without anterior coil), MR-linac 2 measurement 1, MR-linac 2 measurement 2 and MR-linac 3 measurement 1. Figure 10 illustrates small transmission differences between the measured and calculated angular transmission, with transmission differences of $-0.02\% \pm 0.59\%$ (mean + standard deviation), $0.06\% \pm 0.57\%$, $-0.19\% \pm 0.76\%$, $-0.33\% \pm 0.60\%$, $0.27\% \pm 0.91\%$, for the five datasets, respectively. 92.5%, 93.7%, 87.5%, 77.1% and 87.5% of the datapoints show a transmission difference smaller than 1%, for the five datasets, respectively. The datasets consist of 120, 70, 107, 70 and 120 datapoints. There are larger transmission differences visible at the table (from 125° to 235°) and at the edge of the table (approximately 120° and 240°). Transmission differences up to 4.3% are visible.

4. Discussion

This study gives a comparison between the GPUMCD calculations and measurements, focusing on the sources of uncertainty related to the radiation components of the MR-linac treatment unit. The calculated and measured

(a) Transmission MR-linac 1.

(b) Transmission MR-linac 2.

(c) Transmission MR-linac 3.

Figure 9. Measured, calculated and cryostat transmission relative to the 90° reading.

doses showed good agreement over the range of field sizes, off-axis position, depth and gantry angle considered. Differences between absolute point doses were found to be within 1.7% and the relative dose profiles in the crossline, inline and PDD direction illustrated maximum mean dose differences of 0.9pp, 0.8pp and 0.7pp of D_{max} in the central region for field sizes 2×2 cm² and larger. The maximum mean DTA in the penumbra was 0.7 mm. The mean difference in angular transmission ranged from $-0.33\% \pm 0.60\%$ to $0.27\% \pm 0.91\%$, using multiple treatment machines and datasets. 77.1%–93.7% of the datapoints remained within 1% transmission difference for all three treatment machines. Positions further from the central axis or different field sizes did not cause larger relative dose differences. Our results show that the GPUMCD calculations are consistent with measurements with a low uncertainty. The fields are not only defined by the off-axis output factors, the simulation of the penumbra in particular is dependent on the model of the linac head, (off-axis) energy spectrum, and how transmission through high-density components is implemented in the Monte Carlo code (Sheikh-Bagheri and Rogers 2002, Chetty *et al* 2007). The largest error is caused by the couch transmission and the differences in absolute dose, showing errors up to 4.3% at the edge of the table. The uncertainties in the

Figure 10. Transmission difference of the calculations and measurements. The transmission differences are divided in regions representing transmission difference smaller than 0.5% (white), smaller than 1.0% (light gray) and higher than 1.0% (dark gray).

relative dose profiles are showing a lower uncertainty, with a maximum mean dose difference of 0.9pp of D_{max} between measurements and calculations in the central region. As the outcome of this research prescribes the accuracy of the GPUMCD calculations, this research can be meaningful for all researchers using this dose algorithm. When considering the uncertainty associated with the measurements, these results illustrate that the GPUMCD calculations provide reliable dose calculations with a low uncertainty accurate to $2 \times 2\,\mathrm{cm}^2$ field sizes.

Earlier comparisons between GPUMCD and other algorithms were already performed. Paudel *et al* compared the GPUMCD algorithm with XVMC, CCC, film measurements and ionization measurements and Ahmad *et al* compared the GPUMCD algorithm with GEANT4 (Ahmad *et al* 2016, Paudel *et al* 2016). Both papers showed good agreement of GPUMCD against the other algorithms and methods, this agrees with the outcome of this research. Paudel *et al* showed no clinically significant dose differences between the GPUMCD, XVMC, CCC algorithms and measurements except for the $2 \times 2\,\mathrm{cm}^2$ fields for the CCC algorithm. In this research the $1 \times 1\,\mathrm{cm}^2$ fields are showing larger dose differences and there are no larger dose deviations present at the $2 \times 2\,\mathrm{cm}^2$ fields. This is in line with the research of Ahmad *et al* who also provides reliable dose calculations for all fields, including the $2 \times 2\,\mathrm{cm}^2$ field, with a maximum dose variation along the central axis between GPUMCD and GEANT4 of less than 2% (Paudel *et al* 2016). Friedel *et al* developed an independent MR-linac head and cryostat model in EGSnrc including magnetic field effects for possible secondary dose calculations in the future (Friedel *et al* 2019). They showed good agreement between both the new model in EGSnrc and their watertank measurements and between the new model in EGSnrc and GPUMCD calculations.

In general, the smaller field sizes in the central axis or fields further off-axis showed some larger absolute dose deviations compared to the standard $10 \times 10\,\mathrm{cm}^2$ field size, where no dose difference was present because this field was used for normalisation. However, the dose differences for field sizes $2 \times 2\,\mathrm{cm}^2$ or larger remained within 1.7%. Additionally, there is no clear pattern between field size and/or off-axis position and dose

deviation. Fields further off-axis did not show larger relative dose deviations. This is in line with the research from Mönnich *et al* who developed and implemented an optimized method for QA of treatment plans for a 1.5 T MR-linac using a static solid phantom and a 2D ionization chamber (Mönnich *et al* 2020). Shifts of 11 cm were applied in some of the plans. Smaller off-axis volumes were measured successfully with a median pass rate of 98%, which was comparable to other tumor sites more centrally orientated. However, geometric limitations occured for very large off-axis target volumes, leading to lower pass rates (Mönnich *et al* 2020).

The volume averaging effect (of the Semiflex 3D) and the angular dependency (of the Microdiamond detector) affect the absolute dosimetric outcomes (Woodings *et al* 2018a). For the absolute measurements, a dosimetric comparison between the Microdiamond and Semiflex 3D detectors was perfomed using multiple field sizes and positions. The measurements from the Microdiamond were corrected for the angular dependency caused by the magnetic field. The difference in point dose between these detectors for field sizes larger than 2×2 cm^2 ranged from -0.5% to 0.3%. The Microdiamond detector was therefore used for the final point dose measurements.

The mean relative dose differences in this research are in line with the generally achievable tolerances for 3D TPSs, where it is stated that the achievable tolerance in the central 80% of the beam width on the central axis slice is 1% (Fraass *et al* 1998, Van Dyk *et al* 1999).

In the crossline dose profiles there is a noticeable difference between the measured and calculated dose on the -*x* heel of the penumbra and at the shoulders of the penumbra. The calculated dose is subtly but consistently lower than the measured doses, this is clearly illustrated in figures 4(a) and 6. Similar deviations were observed for both treatment machines and there is no clear explanation for this difference.

The 1×1 cm^2 fields showed large differences between measured and calculated doses. Earlier research already showed the difficulty of small field dosimetry, due to challenges such as high dose gradients and detector volume averaging (Das *et al* 2016). The dose difference for absolute point doses for larger field sizes are small. The absolute point dose differences were larger for the 1×1 cm^2 field sizes, showing differences up to 5.3%. For the small field sizes, the central region is difficult to define. In this research the central region consisted of a minimum of ten data points with a high dose gradient fall-off, therefore higher dose differences were noticeable. The trade-off between more data-points including the penumbra or less datapoints without the penumbra had to be made here. Small positional inaccuracies can result in large apparent differences in dose in these high dose-gradient regions.

The measured angular transmission on the central axis generally showed good agreement with the calculations. Some datasets were measured using only one orientation of the Farmer chamber, while other datasets were measured using the average reading of two datasets. The angular dependence of this chamber has been previously measured as no more than 0.5%, with a combined standard error of 0.3%. There are larger transmission differences visible at the edge of the table (approximately $120°$ and $240°$). A small difference in position could cause large differences due to the geometric uncertainty at the edge of the table. In the clinic it is not recommended to irradiate through the edges of table, however it is not prohibited. In some cases it might be necessary to use beam angles through the edge of the table due to other constraints, such as sparing of the arms, heart and other organs at risk.

5. Conclusion

This research investigated the system-related uncertainty for GPUMCD calculations over the range of clinically-relevant field configurations and gantry angles. The dose differences between measurements and GPUMCD calculations for (off-axis) fields and angular transmission showed a good agreement. Differences between absolute point doses were found to be within 1.7% and the relative dose profiles in the crossline, inline and PDD direction illustrated maximum mean dose differences of 0.9pp, 0.8pp and 0.7pp of $D_{\max}$. The maximum mean DTA in the penumbra was 0.7 mm. 77.1%–93.7% of the transmission differences remained within 1% transmission difference for all three treatment machines. The largest transmission differences were present at the edges of the table. Consequently, this research showed that the GPUMCD algorithm provides reliable dose calculations with a small uncertainty accurate to 2×2 cm^2 field sizes, focusing on the off-axis fields and angular transmission.

Acknowledgments

ORCID iDs

M van den Dobbelsteen ⓘ https://orcid.org/0000-0002-9671-8062
S Oolbekkink ⓘ https://orcid.org/0000-0002-2948-6134

References

Acharya S *et al* 2016 Online magnetic resonance image guided adaptive radiation therapy: first clinical applications *Int. J. Radiat. Oncol.* * *Biol.* * *Phys.* **94** 394–403

Agnew J, O'Grady F, Young R, Duane S and Budgell G J 2017 Quantification of static magnetic field effects on radiotherapy ionization chambers *Phys. Med. Biol.* **62** 1731–43

Ahmad S B, Sarfehnia A, Paudel M R, Kim A, Hissoiny S, Sahgal A and Keller B 2016 Evaluation of a commercial mri linac based monte carlo dose calculation algorithm with geant 4 *Med. Phys.* **43** 894–907

Bailey D W, Kumaraswamy L, Bakhtiari M, Malhotra H K and Podgorsak M B 2012 Epid dosimetry for pretreatment quality assurance with two commercial systems *J. Appl. Clin. Med. Phys.* **13** 82–99

Chandarana H, Wang H, Tijssen R and Das I J 2018 Emerging role of mri in radiation therapy *J. Magn. Reson. Imaging* **48** 1468–78

Chen X, Paulson E S, Ahunbay E, Sanli A, Klawikowski S and Li X A 2019 Measurement validation of treatment planning for a mr-linac *J. Appl. Clin. Med. Phys.* **20** 28–38

Chetty I J *et al* 2007 Report of the aapm task group no. 105: issues associated with clinical implementation of monte carlo-based photon and electron external beam treatment planning *Med. Phys.* **34** 4818–53

Das I J, Morales J and Francescon P 2016 Small field dosimetry: what have we learnt? *AIP Conf. Proc.* vol 1747 (AIP Publishing LLC) p 060001

Ezzell G A, Galvin J M, Low D, Palta J R, Rosen I, Sharpe M B, Xia P, Xiao Y, Xing L and Yu C X 2003 Guidance document on delivery, treatment planning, and clinical implementation of imrt: report of the imrt subcommittee of the aapm radiation therapy committee *Med. Phys.* **30** 2089–115

Fraass B, Doppke K, Hunt M, Kutcher G, Starkschall G, Stern R and Van Dyke J 1998 American association of physicists in medicine radiation therapy committee task group 53: quality assurance for clinical radiotherapy treatment planning *Med. Phys.* **25** 1773–829

Friedel M, Nachbar M, Mönnich D, Dohm O and Thorwarth D 2019 Development and validation of a 1.5 t mr-linac full accelerator head and cryostat model for monte carlo dose simulations *Med. Phys.* **46** 5304–13

Hackett S, Van Asselen B, Wolthaus J, Kok J, Woodings S, Lagendijk J and Raaymakers B 2016 Consequences of air around an ionization chamber: are existing solid phantoms suitable for reference dosimetry on an mr-linac? *Med. Phys.* **43** 3961–8

Hissoiny S, Ozell B, Bouchard H and Després P 2011b Gpumcd: a new gpu-oriented Monte Carlo dose calculation platform *Med. Phys.* **38** 754–64

Hissoiny S, Raaijmakers A, Ozell B, Després P and Raaymakers B W 2011a Fast dose calculation in magnetic fields with gpumcd *Phys. Med. Biol.* **56** 5119–29

Iakovenko V, Keller B, Sahgal A and Sarfehnia A 2020 Experimental measurement of ionization chamber angular response and associated magnetic field correction factors in mr-linac *Med. Phys.* **47** 1940–8

Jelen U, Dong B, Begg J, Roberts N, Whelan B, Keall P and Liney G 2020 Dosimetric optimization and commissioning of a high field inline mri-linac *Front. Oncol.* **10** 136

Khan A U, Simiele E A, Lotey R, DeWerd L A and Yadav P 2021 Development and evaluation of a geant4-based monte carlo model of a 0.35 t mr-guided radiation therapy (mrgrt) linear accelerator *Med. Phys.* **48** 1967–82

Kontaxis C, Bol G H, Kerkmeijer L G, Lagendijk J J and Raaymakers B W 2017a Fast online replanning for interfraction rotation correction in prostate radiotherapy *Med. Phys.* **44** 5034–42

Kontaxis C, Bol G, Stemkens B, Glitzner M, Prins F, Kerkmeijer L, Lagendijk J and Raaymakers B 2017b Towards fast online intrafraction replanning for free-breathing stereotactic body radiation therapy with the mr-linac *Phys. Med. Biol.* **62** 7233–48

Kontaxis C *et al* 2020 Delivered dose quantification in prostate radiotherapy using online 3d cine imaging and treatment log files on a combined 1.5 t magnetic resonance imaging and linear accelerator system *Phys. Imaging. Radiat. Oncol.* **15** 23–9

Mahmoudi A *et al* 2019 Penumbra reduction technique and factors affecting it in radiotherapy machines-review study *Radiat. Phys. Chem.* **157** 22–7

Mönnich D, Winter J, Nachbar M, Künzel L, Boeke S, Gani C, Dohm O, Zips D and Thorwarth D 2020 Quality assurance of imrt treatment plans for a 1.5 t mr-linac using a 2d ionization chamber array and a static solid phantom *Phys. Med. Biol.* **65** 16NT01

O'Brien D J, Dolan J, Pencea S, Schupp N and Sawakuchi G O 2018 Relative dosimetry with an mr-linac: Response of ion chambers, diamond, and diode detectors for off-axis, depth dose, and output factor measurements *Med. Phys.* **45** 884–97

O'Brien D J and Sawakuchi G O 2017 Monte carlo study of the chamber-phantom air gap effect in a magnetic field *Med. Phys.* **44** 3830–8

Palmans H, Andreo P, Huq M S, Seuntjens J, Christaki K E and Meghzifene A 2018 Dosimetry of small static fields used in external photon beam radiotherapy: summary of trs-483, the iaea-aapm international code of practice for reference and relative dose determination *Med. Phys.* **45** e1123–45

Paudel M R, Kim A, Sarfehnia A, Ahmad S B, Beachey D J, Sahgal A and Keller B M 2016 Experimental evaluation of a gpu-based Monte Carlo dose calculation algorithm in the monaco treatment planning system *J. Appl. Clin. Med. Phys.* **17** 230–41

Raaijmakers A J, Raaymakers B W and Lagendijk J J 2005 Integrating a mri scanner with a 6 mv radiotherapy accelerator: dose increase at tissue-air interfaces in a lateral magnetic field due to returning electrons *Phys. Med. Biol.* **50** 1363–76

Raaijmakers A J, Raaymakers B W and Lagendijk J J 2008 Magnetic-field-induced dose effects in mr-guided radiotherapy systems: dependence on the magnetic field strength *Phys. Med. Biol.* **53** 909–23

Raaymakers B *et al* 2017 First patients treated with a 1.5 t mri-linac: clinical proof of concept of a high-precision, high-field mri guided radiotherapy treatment *Phys. Med. Biol.* **62** L41–50

Roberts D A *et al* 2021 Machine qa for the elekta unity system: A report from the elekta mr-linac consortium *Med. Phys.* **48** e67–85

Sheikh-Bagheri D and Rogers D 2002 Sensitivity of megavoltage photon beam Monte Carlo simulations to electron beam and other parameters *Med. Phys.* **29** 379–90

Smilowitz J B *et al* 2015 Aapm medical physics practice guideline 5. a.: commissioning and qa of treatment planning dose calculationsmegavoltage photon and electron beams *J. Appl. Clin. Med. Phys.* **16** 14–34

Snyder J E, St-Aubin J, Yaddanapudi S, Boczkowski A, Dunkerley D A, Graves S A and Hyer D E 2020 Commissioning of a 1.5 t elekta unity mr-linac: A single institution experience *J. Appl. Clin. Med. Phys.* **21** 160–72

Spindeldreier C, Schrenk O, Bakenecker A, Kawrakow I, Burigo L, Karger C, Greilich S and Pfaffenberger A 2017 Radiation dosimetry in magnetic fields with farmer-type ionization chambers: determination of magnetic field correction factors for different magnetic field strengths and field orientations *Phys. Med. Biol.* **62** 6708–28

Tijssen R H, Philippens M E, Paulson E S, Glitzner M, Chugh B, Wetscherek A, Dubec M, Wang J and van der Heide U A 2019 Mri commissioning of 1.5 t mr-linac systems-a multi-institutional study *Radiother. Oncol.* **132** 114–20

Torres-Xirau I, Olaciregui-Ruiz I, van der Heide U A and Mans A 2019 Two-dimensional epid dosimetry for an mr-linac: proof of concept *Med. Phys.* **46** 4193–203

van den Dobbelsteen M, de Vries W, van Asselen B, Raaymakers B, Woodings S, Oolbekkink S and Hackett S 2022 Po-1743 dosimetric evaluation of off-axis fields and angular transmission for the 1.5 t mr-linac *Radiother. Oncol.* **170** S1544–5

Van Dyk J *et al* 1999 The modern technology of radiation oncology *Medical Physics Publishing* (Madison, WI: University of Wisconsin Press) pp 437–79

Winkel D *et al* 2019 Adaptive radiotherapy: the elekta unity mr-linac concept *Clin. Transl. Radiat. Oncol.* **18** 54–9

Woodings S J *et al* 2018b Beam characterisation of the 1.5 t mri-linac *Phys. Med. Biol.* **63** 085015

Woodings S J, Wolthaus J W, van Asselen B, De Vries J, Kok J G, Lagendijk J and Raaymakers B W 2018a Performance of a ptw 60 019 microdiamond detector in a 1.5 t mri-linac *Phys. Med. Biol.* **63** 05NT04

Zhang K, Tian Y, Li M, Men K and Dai J 2021 Performance of a multileaf collimator system for a 1.5 t mr-linac *Med. Phys.* **48** 546–55

Zwan B J, Barnes M P, Hindmarsh J, Lim S B, Lovelock D M, Fuangrod T, O'Connor D J, Keall P J and Greer P B 2017 Commissioning and quality assurance for vmat delivery systems: an efficient time-resolved system using real-time epid imaging *Med. Phys.* **44** 3909–22